ADVANCED MATERIALS INTERFACES
www.advmatinterfaces.de

Mn_3O_4 Nanomaterials Functionalized with Fe_2O_3 and ZnO: Fabrication, Characterization, and Ammonia Sensing Properties

Lorenzo Bigiani, Dario Zappa, Chiara Maccato, Alberto Gasparotto, Cinzia Sada, Elisabetta Comini, and Davide Barreca**

The fabrication of metal oxide-based gas sensors with tailored structural design is of particular importance for the early recognition of poisonous/explosive analytes like ammonia, an irritating chemical occurring in a plethora of practical contexts. In this regard, the present work reports on the fabrication and gas sensing application of p-Mn_3O_4/n-M_xO_y nanocomposites with M_xO_y = Fe_2O_3 or ZnO. The target systems are developed by chemical vapor deposition of Mn_3O_4 nanosystems on alumina substrates and subsequent functionalization with iron or zinc oxides by sputtering under mild conditions. Material characterization reveals the formation of high purity composites with a controllable dispersion of Fe_2O_3 or ZnO into Mn_3O_4, and a close contact between the single constituents. The latter feature, resulting in the formation of p-n junctions and in a tailored modulation of Mn_3O_4 hole accumulation layer, is of strategic importance in obtaining promising responses to ammonia already at moderate temperatures. Furthermore, Fe_2O_3 or ZnO functionalization empowers the pristine Mn_3O_4 with good selectivity toward NH_3 against other potential interferents. These results, along with the very favorable detection limits, provide new physical insights for the implementation of gas-sensitive devices with p-n junctions aimed at practical end uses.

1. Introduction

Conductometric gas sensors based on metal oxides offer manifold advantages in view of applications in environmental monitoring, citizen security, and medical diagnosis, encompassing low cost, limited power consumption, reduced size/weight, good stability, and sensitivity to harmful compounds.[1–12] In particular, nanostructured metal oxides are promising sensing materials thanks to their favorable chemical reactivity and large surface-to-volume ratio, which provides a high active area for the interaction with the target analytes.[13–19] Over the last decade, various efforts have been dedicated to the efficient recognition of toxic/explosive chemicals, among which ammonia,[20] an irritating agent occurring in fertilizing manufacturing, in refrigerants, and in medical/industrial contexts,[8,21–23] may represent a serious threat for both environment and human health. In this regard, whereas various n-type semiconducting oxides have been proposed for ammonia detection, NH_3 sensors based on p-type materials have been only scarcely investigated.[20] Nonetheless, despite the research on p-type oxide gas sensors remains poorly explored,[24–27] such systems hold a considerable promise for high-performance gas sensitive devices with new functions, thanks to their affinity with oxygen, high catalytic activity, and multivalent characteristics.[17,24,28]

Among p-type oxides, Mn_3O_4 has drawn a considerable scientific interest as a model spinel thanks to its low cost, environmental compatibility, and unique chemico-physical properties, that render it an attractive candidate for various end uses.[5,14,26,29–32] Despite various studies have reported on the use of pure/doped Mn_3O_4 for gas sensing applications,[14–16,33] important issues to be still addressed are related to the ever increasing request for enhanced sensitivity, stability, and selectivity,[3,24,29,30] the well-known "3S" of a gas sensor.[2] In this context, a valuable option is offered by the fabrication of nanocomposites based on p-type Mn_3O_4 and suitable n-type oxides, since the controlled formation of oxide-oxide p-n junctions can extend the space charge region, yielding improved functional performances.[24,30,34–36] So far, literature reports on Mn_3O_4-based

Dr. L. Bigiani, Prof. C. Maccato, Prof. A. Gasparotto
Department of Chemical Sciences
Padova University and INSTM
35131 Padova, Italy
E-mail: chiara.maccato@unipd.it
Dr. D. Zappa, Prof. E. Comini
Sensor Lab
Department of Information Engineering
Brescia University
25133 Brescia, Italy
Prof. C. Sada
Department of Physics and Astronomy
Padova University and INSTM
35131 Padova, Italy
Dr. D. Barreca
CNR-ICMATE and INSTM
Department of Chemical Sciences
Padova University
35131 Padova, Italy
E-mail: davide.barreca@unipd.it
The ORCID identification number(s) for the author(s) of this article can be found under https://doi.org/10.1002/admi.201901239.

DOI: 10.1002/admi.201901239

composite chemoresistors are limited[5,29,30,37] and in particular, to the best of our knowledge, only three works on ammonia detection by bare Mn_3O_4,[16] Ba-doped Mn_3O_4,[26] and Mn_3O_4-decorated ZnO[30] are available to date. As a consequence, the development and implementation of Mn_3O_4-based ammonia sensors with enhanced performances deserve further investigation from both a fundamental and an applicative point of view.

The results obtained in the present work aim at filling this gap, disclosing the possibility of achieving an efficient and selective ammonia recognition through the use of p-Mn_3O_4/n-M_xO_y (M_xO_y = Fe_2O_3 or ZnO) nanocomposites. The rationale of this approach lies in the exploitation of multivalence properties and synergistic electronic/catalytic effects between p-type Mn_3O_4 and n-type modifiers to achieve improved sensing performances at moderate temperatures, an issue of key importance for eventual practical applications.[34] The choice of Fe_2O_3 is mainly motivated by its interest in finding new functionalities in chemoresistivity, whereas ZnO, a very attractive multifunctional oxide,[38] belongs to the most representative sensor materials.[19,24,34,35,39] In particular, Mn_3O_4/M_xO_y nanosystems were obtained by the initial chemical vapor deposition (CVD) of Mn_3O_4 on Al_2O_3 substrates, followed by the functionalization with Fe_2O_3 or ZnO under controlled conditions. The latter process was conducted by radio frequency (RF)-sputtering at low temperatures and applied powers, to avoid detrimental alterations of the pristine Mn_3O_4 systems and enable a direct control on the resulting composite characteristics.[36,40] After a morphological, compositional, and structural characterization, the target materials are utilized for the fabrication of chemoresistive gas sensors for ammonia. The results demonstrate that the prepared systems can efficiently detect NH_3 and discriminate it with respect to other N-containing volatile compounds acting as potential interferents, namely CH_3CN, a toxic gas, simulant of cyanide warfare agents,[1,3,41,42] and NO_2, a dangerous atmospheric pollutant.[2,4,17] The interplay between the system behavior and material properties is critically discussed in relation to a possible gas sensing mechanism highlighting the role of p-n junctions and hole accumulation layer (HAL) modulation in boosting functional performances. This study can provide an important guide for the functionalization of oxide systems aimed at improving sensitivity and selectivity, and sheds new light on material design to develop chemoresistive gas sensors for NH_3 detection.

2. Results and Discussion

2.1. Material Characterization

On the basis of our previous results,[28,41] the synthesis of single-phase Mn_3O_4 nanosystems was carried out by CVD under optimized conditions, with particular attention to the fabrication of porous deposits for the subsequent overdispersion of Fe and Zn oxides. The system morphology was characterized by field emission-scanning electron microscopy (FE-SEM) analyses (**Figure 1**), revealing a uniform distribution of faceted grains with comparable sizes for the target specimens (average dimensions = [150 ± 50] nm and [160 ± 40] nm for Mn_3O_4/Fe_2O_3 and Mn_3O_4/ZnO, respectively). These particles were assembled into a porous deposit (mean thickness = 510 nm) conformally covering the underlying Al_2O_3 substrates. A comparison of the present results with bare Mn_3O_4 (Figure S1, Supporting Information) evidenced that, after iron and zinc oxide deposition, no significant morphological alterations took place. This result, achieved thanks to the use of particularly mild sputtering conditions, is in line with previous data regarding CuO-TiO_2-Au nanomaterials.[36] The inherent material porosity suggested the occurrence of a high contact area with the outer atmosphere, a beneficial feature for gas sensing applications.[15,18,29]

The system composition was preliminarily investigated by energy dispersive X-ray spectroscopy (EDXS). The recorded spectra were dominated by the oxygen and manganese X-ray lines, along with the Al signal from the alumina substrate. Whereas for Mn_3O_4/Fe_2O_3 no iron peak could be unambiguously detected due to the energy position very close to Mn, for Mn_3O_4/ZnO the Zn Lα signal at 1.0 keV could be observed (Figure S2, Supporting Information). Morphological characterization of the target materials after 1 year did not show any significant variation in the mean grain sizes (Figure S3, Supporting Information). Important information on the system surface composition and Mn, Fe, and Zn chemical states was gained by X-ray photoelectron spectroscopy (XPS). For all specimens, spectra revealed the presence of O and Mn, along with iron/zinc photoelectron and Auger signals for composite systems. A minor contribution from carbon (<10 atomic percentage [at%]) was traced back to atmospheric exposure. For pure Mn_3O_4, the $Mn2p_{3/2}$ peak shape and position (**Figure 2**a; $Mn2p_{3/2}$ binding energy [BE] = 641.8 eV, spin-orbit splitting [SOS] = 11.5 eV), along with its BE difference with respect to the O1s lattice component (see below; Δ = 111.8 eV), were in line with previous literature reports.[16,31,32,40,43] A careful data analysis revealed that the $Mn2p_{3/2}$ BE underwent a progressive shift toward lower values upon going from bare Mn_3O_4 (641.8 eV) to Mn_3O_4/Fe_2O_3 (641.6 eV) and, finally, to Mn_3O_4/ZnO (641.3 eV). This phenomenon could be explained basing on the formation

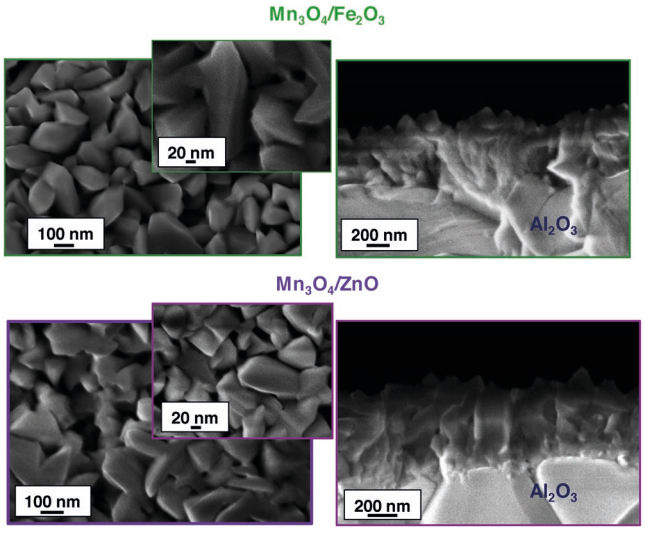

Figure 1. Representative plane-view and cross-sectional FE-SEM micrographs for Mn_3O_4/Fe_2O_3 and Mn_3O_4/ZnO specimens.

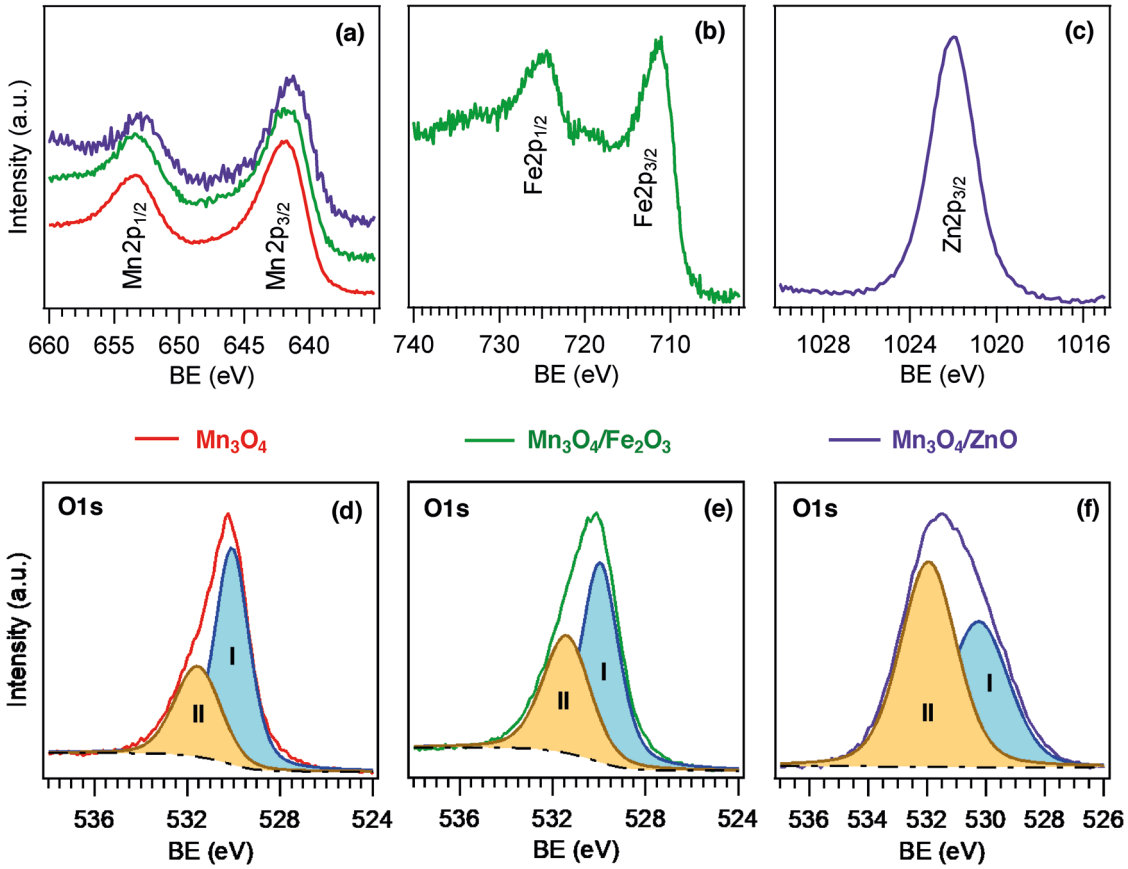

Figure 2. Surface a) Mn2p, b) Fe2p, c) $Zn2p_{3/2}$, and O1s XP spectra for d) Mn_3O_4, e) Mn_3O_4/Fe_2O_3, and f) Mn_3O_4/ZnO samples.

of p-n junctions at Mn_3O_4/M_xO_y interfaces, yielding an electron transfer from n-type M_xO_y to p-type Mn_3O_4, with holes moving in the opposite direction.[7,17,29,44]

The fact that the $Mn2p_{3/2}$ BE shift is more pronounced for the ZnO-containing specimen highlights a more efficient charge transfer at the Mn_3O_4/ZnO interface with respect to the Mn_3O_4/Fe_2O_3 one, a feature positively impacting the eventual sensing performances (see below). In accordance with the above observations, the $Fe2p_{3/2}$ and $Zn2p_{3/2}$ energy positions (Figure 2b,c; BE($Fe2p_{3/2}$) = 711.4 eV and BE($Zn2p_{3/2}$) = 1022.0 eV) were slightly higher than those reported in the literature for Fe_2O_3[45,46] and ZnO,[34] respectively. In any case, the presence of the latter, free from other zinc-containing phases, was confirmed by the Zn Auger parameter (α = 2010.0 eV).[35,47] In addition, the Mn3s multiplet splitting separation (5.5 eV, Figure S4, Supporting Information) provided a finger-print for the occurrence of pure Mn_3O_4.[40,41,48] These results enabled to discard the presence of other Mn-M-O ternary systems (M = Fe, Zn), consistently with X-ray diffraction (XRD) data, indicating that the single oxides preserved their chemical identity.

Additional information was gained by the analysis of the O1s XPS peaks (Figure 2d–f), which resulted from the concurrence of two bands at BE values of 530.1 eV (**I**), corresponding to lattice oxygen, and 531.6 eV (**II**), due to surface adsorbed oxygen species.[10,17,45,48,49] The contribution of this second component to the total O content was estimated to be 34.0%, 41.2%, and 57.6% for Mn_3O_4, Mn_3O_4/Fe_2O_3, and Mn_3O_4/ZnO specimens, respectively, becoming progressively more abundant and, ultimately, predominant in the latter case. The different amounts of adsorbed oxygen species in the target systems is expected to produce a diverse functional behavior in gas sensing processes. In fact, the increasing oxygen defect content observed for composite systems, in particular for ZnO-containing ones, is responsible for a more efficient adsorption of both oxygen species and the analyte gas, resulting in a higher detection efficiency[22,28,29] (see below).

To obtain complementary compositional information on the in-depth mutual Mn_3O_4/M_xO_y distribution, secondary ion mass spectrometry (SIMS) characterization was undertaken. For both specimens, C content was lower than 100 ppm, indicating a good specimen purity. Regardless of the adopted processing conditions, the recorded profiles (**Figure 3**) displayed qualitatively similar features. O ionic yields were almost constant throughout the sampled thickness, and the relatively broad deposit/alumina interface was ascribed to the inherent Al_2O_3 substrate roughness.[28] Mn and M (M = Fe, Zn) exhibited an almost parallel trend, indicating a uniform in-depth composition. These data highlighted an effective M_xO_y dispersion within the pristine Mn_3O_4 network. Since functionalization with Fe_2O_3 and ZnO by RF-sputtering was performed at 60 °C, appreciable thermal effects could be excluded, and the in-depth intimate Mn_3O_4/M_xO_y contact was traced back to the synergy between manganese oxide porosity and the infiltration power ensured by RF-sputtering.[36,40] This result

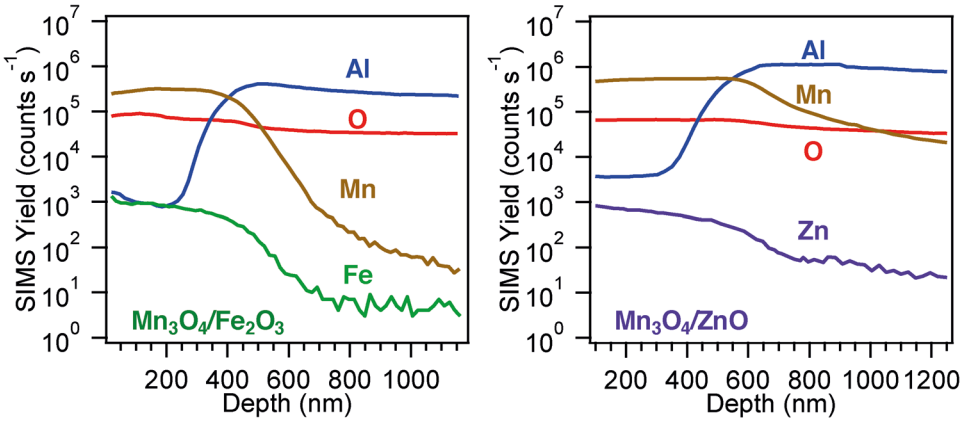

Figure 3. SIMS depth profiles for Mn_3O_4/Fe_2O_3 and Mn_3O_4/ZnO specimens.

is of key importance in determining the ultimate sensing performances.

Microstructural information was gained by XRD (**Figure 4**). The obtained results indicated the polycrystalline structure of the analyzed materials, and all the diffraction peaks could be indexed to the spinel structure of α-Mn_3O_4 (*haussmannite*).[50] No signals related to impurities or to other manganese oxides were observed in the XRD patterns. Functionalization with Fe_2O_3 or ZnO did not yield additional reflections with respect to the pristine Mn_3O_4 and any appreciable Mn_3O_4 peak shift with respect to the reference pattern, enabling to discard the occurrence of significant structural modifications. The absence of reflections related to Fe_2O_3 or ZnO could be ascribed to their relatively low amount, small crystallite size, and high dispersion in the Mn_3O_4 deposits,[35,36] the latter feature being clearly evidenced by SIMS analyses. The average Mn_3O_4 crystallite dimensions were estimated to be 35 nm for all the investigated systems.

2.2. Gas Sensing Properties

Gas sensing tests on the developed materials evidenced a good reproducibility up to 3 months of prolonged use without any appreciable deterioration, an important characteristic for practical applications.[28] The system functional behavior was initially screened toward CH_3CN, NO_2 and NH_3 as a function of the adopted working temperature. **Figure 5** displays an overview of sensing responses to selected concentrations of nitrogen-containing volatile compounds for bare and functionalized Mn_3O_4 nanosystems under different conditions. As can be observed, a drastic selectivity pattern change took place upon going from bare manganese oxide to functionalized systems. In fact, in line with previous data, pure Mn_3O_4 sensors enabled acetonitrile discrimination with respect to NO_2 and NH_3.[16,28,29] Conversely, functionalization of the sensor surface and the judicious choice of the operational temperature resulted in an ammonia detection efficiency considerably exceeding the ones of acetonitrile and nitrogen dioxide. The ratio between the responses to ammonia and to interfering gases (CH_3CN or NO_2) was calculated as a measure of gas selectivity,[24] yielding values ≥16.0 and 20.0 for Mn_3O_4/Fe_2O_3 and Mn_3O_4/ZnO, respectively, at a temperature of 300 °C. This result is an important prerequisite to avoid false alarms for practical applications

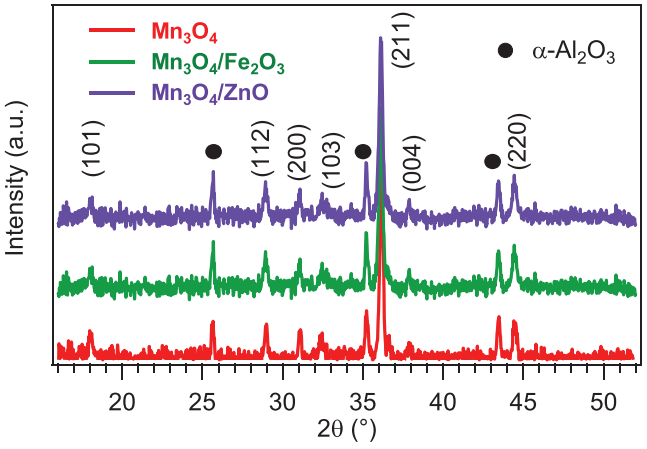

Figure 4. XRD patterns for bare and functionalized Mn_3O_4 nanosystems.

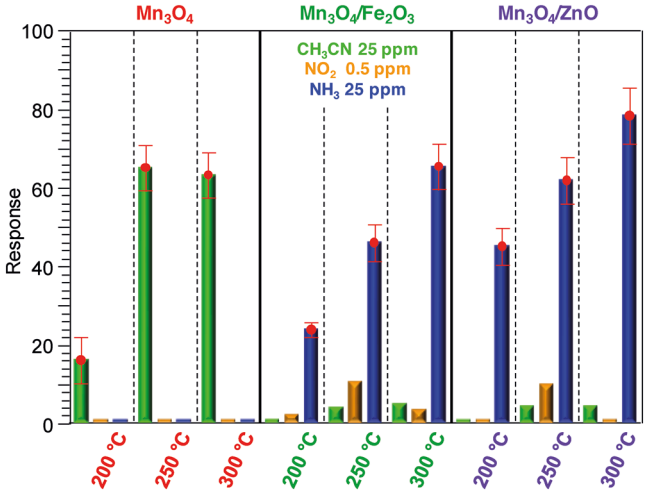

Figure 5. Responses of Mn_3O_4, Mn_3O_4/Fe_2O_3, and Mn_3O_4/ZnO sensors to selected analyte concentrations as a function of the operating temperature.

in real-time gas monitoring equipments aimed at detecting ammonia leakages.[17,35]

In general, a rationale of the observed selectivity is not straightforward, since this property is directly influenced by the concurrence of material composition and of the corresponding chemico-physical characteristics, including morphology and nature of the active sites.[5,28] In this case, the negligible responses to NO_2 could be explained considering that materials based on p-type Mn_3O_4 are oxidation catalysts, hindering thus an efficient detection of oxidizing analytes like nitrogen dioxide.[24] In a different way, CH_3CN sensing was significantly affected by the nature of the active materials, and Figure 5 shows that the responses to this gas were suppressed by functionalization with Fe_2O_3 or ZnO. This phenomenon suggested that acetonitrile surface activation is directly dependent on the nature and distribution of the active surface sites. A tentative explanation in this regard could arise by the fact that CH_3CN oxidation, involving the release of a high number of electrons, is a complex process often conducted under relatively harsh conditions,[42] and is best promoted by a stronger oxidizing agent. Basing on the above XPS data, bare Mn_3O_4, for which the Mn2p energy position is higher with respect to Mn_3O_4/M_xO_y systems, suggesting thus the occurrence of more acidic Mn surface sites, is likely more suited than the targeted composites to promote acetonitrile surface reaction and subsequent recognition. Nevertheless, a thorough clarification of the reasons underlying the observed behavior would require additional and deeper mechanistic studies.

For ammonia detection by Mn_3O_4/Fe_2O_3 and Mn_3O_4/ZnO specimens, the responses to NH_3 underwent a progressive enhancement with the working temperature, similarly to NiO-based sensors under similar operational conditions.[20,21] Such a result suggested that the reactions between the analyte and chemisorbed oxygen species (see below) were thermally activated.[5,28,35,41] The optimal performances were recorded at 300 °C, a working temperature lower than the best one usually reported for ammonia detection by ZnO and SnO_2-based sensors,[8,51] as well as Ba-doped Mn_3O_4 systems.[26]

Notably, the best responses to NH_3 recorded in the present study for Mn_3O_4/ZnO nanomaterials outperformed the ones to analogous ammonia concentrations reported in the literature for MoS_2/Co_3O_4 nanocomposites,[52] as well as for other sensing materials based on NiO films and composites,[17,20] MoO_3 nanostructures,[10] $AgAlO_2$,[8] Co_3O_4, CuO, Co_3O_4/CuO, SnO_2 nanomaterials,[11,25] In_2O_3-TiO_2 composites,[53] and reduced graphene oxide composites with Zn, Ti and Cu(I) oxides.[22,52] This result highlights that the developed Mn_3O_4/ZnO nanocomposites are attractive candidates for constructing high-performance ammonia sensors for various applications.[52]

Figure 6 and Figure S5, Supporting Information, display the isothermal dynamic responses to ammonia for nanocomposite systems and for bare Mn_3O_4, respectively. A comparison of the reported data further evidenced that bare Mn_3O_4 was almost insensitive to this analyte, as already discussed. Conversely, the developed composites were sensitive to NH_3 exposure, and the conductance decrease observed upon contact with this reducing agent highlighted a p-type behavior[26,29,33] for both Fe_2O_3- and ZnO-containing nanocomposites. This finding, in accordance with the presence of Mn_3O_4 as the dominant

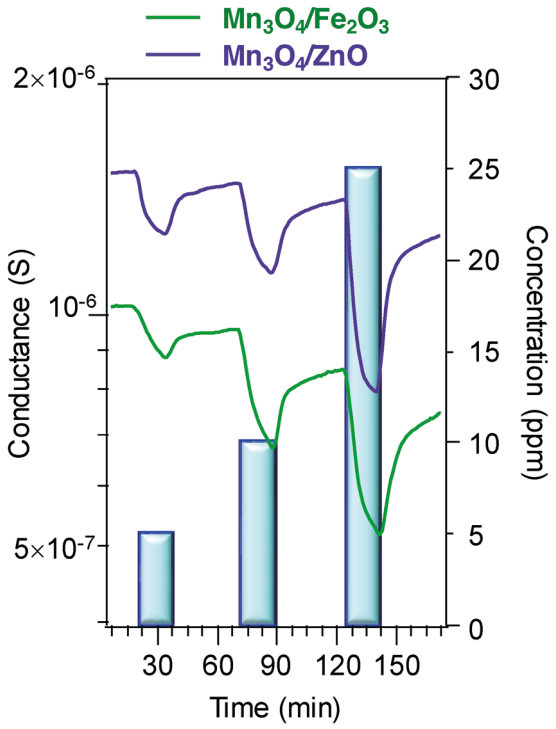

Figure 6. Dynamic responses exhibited by Mn_3O_4/Fe_2O_3 and Mn_3O_4/ZnO nanosystems at a working temperature of 300 °C toward a sequence of NH_3 concentrations pulses. The minimum concentration used for NH_3 was the human odor threshold (5 ppm).[54]

phase, suggested that the conduction occurred through the p-type Mn_3O_4 network rather than n-type Fe_2O_3 or ZnO.[29] As can be observed, despite the incomplete baseline recovery after ammonia pulses (**Figure 6**), the measured conductance variations were proportional to the used NH_3 concentrations, without any significant saturation effect. In line with literature data for Mn_3O_4 sensors,[15,28,33,41] the rapid conductance drop-off upon gas exposure was followed by a slower variation up to the end of each gas pulse, indicating that analyte chemisorption onto the sensor surface was the rate-limiting step in the resulting current change.[28,36,41]

In general, the chemoresistor response/recovery kinetics arise from the combination of different phenomena, including gas diffusion and chemical reactions between gaseous molecules impinging over the sensor and the reactive sites available on its surface.[2] The response and recovery times obtained in the present work compared favorably with literature values for CuO nanowires[25] and MoS_2/Co_3O_4 nanocomposites.[52] For an ammonia concentration of 25 ppm, τ_{resp} and τ_{rec}, calculated at the best operating temperature (300 °C), were 2 and 30 min for Mn_3O_4/Fe_2O_3, and decreased to 1 and 16 min for Mn_3O_4/ZnO. This difference between Mn_3O_4/Fe_2O_3 and Mn_3O_4/ZnO highlighted the better functional performances of the latter, as already anticipated and evidenced by a comparison of the pertaining curves in Figure 6. The relatively slow reversal to air conductance upon switching off gas pulses could be traced back to the sluggish out-diffusion recovery processes, as well as to the slow desorption kinetics of reaction products at the adopted temperatures.[28,41]

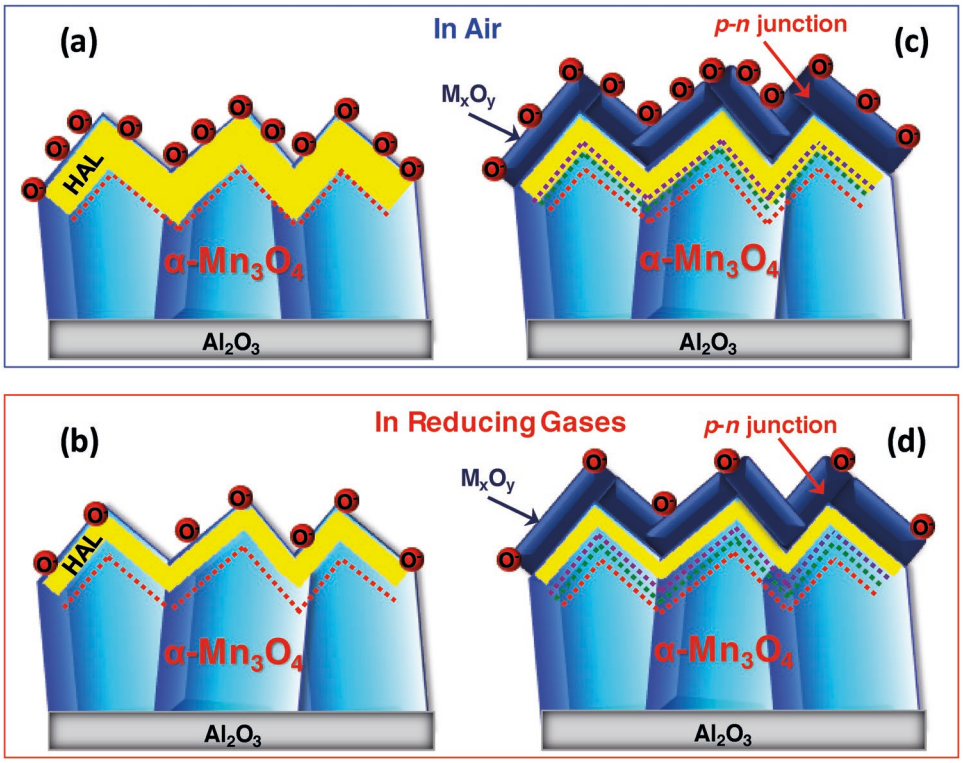

Figure 7. Sketch of the ammonia gas sensing mechanism occurring for the target Mn_3O_4-based systems. a) HAL generation in bare Mn_3O_4 after air exposure and b) subsequent modulation upon contact with ammonia. Panels c) and d) represent the analogous phenomena for Mn_3O_4/M_xO_y nanocomposites. The dashed red, green, and violet lines mark the HAL boundary for pure Mn_3O_4, Mn_3O_4/Fe_2O_3, and Mn_3O_4/ZnO, respectively.

As a matter of fact, the comprehension of the surface chemistry of pollutant analytes on oxide sensors is crucial to improve device performances.[25] The observed current variations (Figure 6 and Figure S5, Supporting Information) can be discussed in relation to a possible NH_3 sensing mechanism. When the sensor surface is initially in contact with air, O_2 chemisorption generates active oxygen species by electron capture:[6,15,22,27,39,52,55]

$$O_{2(g)} \rightleftarrows O_2^- \rightleftarrows 2O^- \rightleftarrows 2O^{2-} \quad (1)$$

The involved electron transfer from the material to chemisorbed oxygen results in the build-up of a low-resistance HAL in the proximity of material surface[5,11,18,23,24] (**Figure 7**a for bare Mn_3O_4; HAL thickness = 20.6 nm, see the Supporting Information). The subsequent interaction of the sensor surface with ammonia can be described as follows:[20,25,26,54]

$$4NH_3 + 3O_2^- \rightleftarrows 2N_2 + 6H_2O + 3e^- \quad (2)$$

$$2NH_3 + 3O^- \rightleftarrows N_2 + 3H_2O + 3e^- \quad (3)$$

$$2NH_3 + 3O^{2-} \rightleftarrows N_2 + 3H_2O + 6e^- \quad (4)$$

The consumption of ionosorbed oxygen, yielding N_2 and H_2O as the main reaction products and a concomitant electron release into the conduction band of the sensor material, is responsible for a lowered hole concentration,[8,28,41] resulting in a reduced HAL width (Figure 7b for bare Mn_3O_4) and the consequent modulation of the sensor electrical conductance (Figure 6).[19–21] Finally, at the end of gas pulse, the initial situation in air is restored.

How to account for the beneficial role of composite systems on the sensor functional behavior? As already mentioned, the presence of p–n Mn_3O_4/M_xO_y junctions, demonstrated by XPS analysis (see above), produces an interfacial electron transfer toward Mn_3O_4.[7,17,29,44] The concomitant hole flow toward M_xO_y accounts for the modulation in the HAL thickness with respect to the bare Mn_3O_4 sensor (compare Figure 7a and 7c; HAL thickness = 19.5 nm and 18.5 nm for Mn_3O_4/Fe_2O_3 and Mn_3O_4/ZnO junctions, respectively, see the Supporting Information). Variations of the latter upon ammonia exposure yields thus higher sensing responses for Mn_3O_4/M_xO_y composites by enhancing the relative modulations of the measured conductance (compare Figure 7b and 7d).[7,34,55] Nevertheless, the occurrence of cooperative effects in the chemical reactivity of the two oxides can also provide synergistical benefits,[29,35] considering that both Mn_3O_4 and the considered M_xO_y systems are well-known catalytic materials[4,24,28,40,41] capable of promoting the chemical reactions involved in the sensing process. This concurrent contribution can reinforce the sensing performances of Mn_3O_4 composites, whose remarkably higher NH_3 detection efficiency with respect to bare Mn_3O_4 (Figure 6 and Figure S5, Supporting Information) can be related to both electronic and catalytic effects.

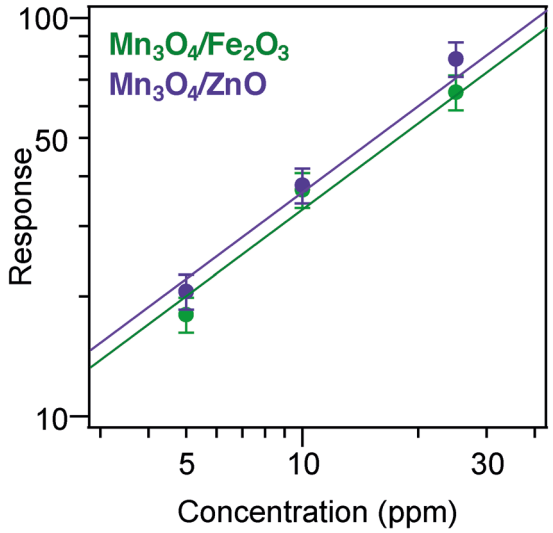

Figure 8. Responses as a function of NH_3 concentration for Mn_3O_4/Fe_2O_3 and Mn_3O_4/ZnO specimens (operating temperature = 300 °C).

The different functional behavior of the two examined composite systems, and, in particular, the higher responses always exhibited by Mn_3O_4/ZnO sensor with respect to the homologous Mn_3O_4/Fe_2O_3 one (see also **Figure 8**), are consistent with the fact that ZnO is one of the best performing gas sensing materials toward a broad category of analytes.[4,24,35] In particular, the improved performances of Mn_3O_4/ZnO could be explained taking into account that the latter featured a higher oxygen defect content (as evidenced by XPS)[56] and induced a higher HAL thickness modulation (see above), favorable characteristics for gas sensing. Nevertheless, it is worthwhile observing that the synergistic Mn_3O_4–M_xO_y interactions can be affected in a complex way by various parameters, including the system morphology and the defect/active site contents, resulting, in turn, in different catalytic activities. Hence, the actual performances arise from a delicate balance of various effects, and the identification of their relative weight is indeed a challenging task deserving additional investigation.

The responses of Mn_3O_4-based composites as a function of ammonia concentration are plotted in Figure 8 at the optimal working temperature. At variance with results for MoS_2/Co_3O_4,[52] Mn_3O_4, Ba-doped Mn_3O_4,[26] and SnO_2-based sensors,[51] the experimental data show a clear linear relationship in the log-log scale (Equation (6)), which enabled to discard significant saturation phenomena, an important issue for quantitative detection.[35,36] Extrapolation of detection limits yielded 2.3 and 2.0 ppm for Mn_3O_4/Fe_2O_3 and Mn_3O_4/ZnO, respectively. Notably, these values are one order of magnitude lower than the NH_3 threshold limit (toxicity) recommended by the Occupational Safety and Health Administration (OSHA), that is, 25 ppm, and the maximum allowable NH_3 concentration indicated by the "Health standards for industrial enterprises" (TJ 36–79) of China (40 ppm).[8,19–22] The sensing capability of the present systems is further highlighted by a comparison with literature works on chemoresistive NH_3 detection, evidencing a much higher sensitivity than MoS_2, reduced graphene oxide composites with Co, Zn, Ti and Cu(I) oxides,[52] $AgAlO_2$,[8] ZnO nanorods, SnO_2 composites, NiO, WO_3, and CeO_2-based sensors.[20,49]

3. Conclusion

In the present work, p-Mn_3O_4/n-M_xO_y nanocomposites (M_xO_y = Fe_2O_3 or ZnO) for ammonia sensing were prepared for the first time by means of a hybrid vapor phase approach. The proposed route consisted in the initial CVD of Mn_3O_4 nanosystems on alumina substrates, yielding high area nanodeposits which were subsequently functionalized with Fe_2O_3 or ZnO by RF-sputtering. The obtained results highlight the successful fabrication of high purity Mn_3O_4/Fe_2O_3 and Mn_3O_4/ZnO nanocomposites featuring a close contact between the single-phase oxide constituents. For the first time, the obtained systems were tested as conductometric sensors for the recognition of gaseous ammonia against other N-containing species (acetonitrile, nitrogen dioxide). Data analysis disclosed attractive responses at moderate temperatures and good selectivity toward NH_3, together with detection limits appreciably lower than the ammonia threshold allowed by safety regulations. The analysis of the system behavior suggested that the chemical-to-electrical transduction mechanism was dominated by the presence of p-n junctions and a tailored modulation of the Mn_3O_4 hole accumulation layer. Thanks to the promising performances, the good response/recovery times, as well as to the low material cost and limited power consumption, the developed systems stand as interesting platforms to selectively control the ammonia level in environmental monitoring, medical diagnostics, human health protection, and public security. Basing on the presently reported results, our future attention will be dedicated to an additional optimization of the system performances, with particular regard to the sensor stability, to be investigated in detail by compositional analyses even after sensing tests.

4. Experimental Section

Synthesis: Mn_3O_4 nanosystems were prepared using a custom-built cold-wall horizontal CVD reaction system with an external precursor reservoir. Depositions were carried out on pre-cleaned[28,41] polycrystalline Al_2O_3 substrates (Maruwa, 99.6%; size = 3 × 3 mm^2; thickness = 250 µm), using Mn(hfa)$_2$•TMEDA (hfa = 1,1,1,5,5,5-hexafluoro-2,4-pentanedionate; TMEDA = *N*,*N*,*N*′,*N*′-tetramethylethylenediamine)[48] as manganese molecular source. The precursor powders were vaporized at 60 °C and transported toward the deposition zone by an O_2 flow (purity = 6.0; rate = 100 standard cubic centimetres per minute [sccm]) through gas lines heated at 100 °C. An additional oxygen flow (100 sccm) was separately introduced into the reaction chamber. Following previously obtained results,[28,41] depositions were performed for 1 h at a working pressure of 10.0 mbar, using a substrate temperature of 500 °C. For nanocomposite fabrication, as-prepared specimens were subsequently transferred into a plasmochemical instrumentation (ν = 13.56 MHz). RF-sputtering was carried out from Ar (purity = 5.0) plasmas using iron or zinc targets (Fe: Alfa Aesar, 99.995%; 50 × 50 mm, thickness = 0.250 mm; Zn: Neyco, 99.99%; diameter = 2 in., thickness = 1 mm). After an initial prescreening of the operating conditions, sputtering processes were carried out at a pressure of 0.3 mbar using a RF-power of 20 W, with process durations of 3 and 2 h for iron and zinc sputtering, respectively. No ex

situ annealing was carried out, in order to avoid Mn_3O_4 conversion into other manganese oxides.[43]

Characterization: FE-SEM characterization was performed using a Zeiss SUPRA 40VP instrument equipped with an Oxford INCA x-sight X-ray detector for EDXS analyses, at primary beam acceleration voltages of 10–20 kV. The average deposit thickness and particle size were estimated through various measurements using the ImageJ software (https://imagej.nih.gov/ij/, accessed December 2018).

XPS characterization was carried out by a Perkin–Elmer Φ 5600-ci spectrometer, using a non-monochromatic Al Kα X-ray source (1486.6 eV). The BE values (uncertainty = ±0.2 eV) were corrected for charging by assigning to the C1s peak associated with adventitious hydrocarbons a value of 284.8 eV.[47] At% values were determined after a Shirley-type background subtraction[57] by peak area integration using Φ V5.4A sensitivity factors. The zinc Auger parameter (α) was calculated as previously reported.[45,47]

SIMS analyses were performed by an IMS 4f mass spectrometer (Cameca, Padova, Italy) using a Cs^+ primary beam (20 nA, 14.5 keV; stability = 0.2%), rastering over a nominal 175 × 175 μm^2 area and collecting negative secondary ions from a 7 × 7 μm^2 region to avoid crater effects. Beam-blanking mode was used to improve the depth resolution, interrupting the sputtering process during magnet stabilization periods. Measurements were carried out in high mass resolution configuration to avoid mass-interference artefacts, using an electron gun for charge compensation. The sputtering time in the abscissa of the recorded profiles was converted into depth basing on the deposit thickness values measured by FE-SEM analyses.

XRD measurements were run on a Bruker D8 Advance diffractometer equipped with a Göbel mirror, employing a Cu X-ray tube (40 kV, 40 mA), using an incidence angle of 1.0°. The average crystallite sizes were estimated by the Scherrer equation.[14,15,26,39]

Gas Sensing Tests: Gas sensing responses were tested using the flow-through method in a thermostatic chamber with controlled temperature and relative humidity level (20 °C and 40%, respectively). Interdigitated Pt contacts and a Pt heater were deposited by sputtering on the top of the sensing material and on the Al_2O_3 substrates backside, respectively. Measurements were carried out at temperatures ≤300 °C in order to avoid detrimental Mn_3O_4 alterations,[28,41] stabilizing the sensors for 8 h at each temperature prior to analyte exposure. The total air carrier flow was set at 300 sccm. A fixed voltage (1 V) was applied to the sensors and resistance variations were monitored as a function of gas concentration. The sensor response was defined as:[9,20,23,28,52]

$$\text{Response} = \left(X_g - X_a\right) \times 100/X_a \quad (5)$$

where X_a and X_g indicate, respectively, the resistance (conductance) in air and the values reached after contact with NH_3/CH_3CN (NO_2) analytes. Response/recovery times (τ_{resp}/τ_{rec}; uncertainty = ±10%) were determined as previously reported.[36,41] Response versus concentration trends were fitted by the usual power law relation for metal oxide sensors:[19,21,25,44]

$$\text{Response} = K \times C^B \quad (6)$$

where K and B are constants typical of the active material and the involved reactions.[54] The obtained best fitting parameters are reported in Table S1, Supporting Information. Assuming the validity of the obtained trends even at low gas concentrations, detection limits were extrapolated.

The present nanocomposite sensors did not evidence any significant short-term drifts in the baseline conductance upon testing up to 12 h. Measurements on up to eight identical sensors under the same operating conditions, and even after cycled tests for 1 year (see also Figure S6, Supporting Information), highlighted the device repeatability and stability, yielding a maximum uncertainty of ±5%.

Supporting Information

Supporting Information is available from the Wiley Online Library or from the author.

Acknowledgements

The present research activities received funding from Padova University DOR 2016–2019, P-DiSC #SENSATIONAL BIRD2016-UNIPD, and #03BIRD2018-UNIPD OXYGENA projects, as well as from the INSTM Consortium (INSTMPD010–ISIDE). The authors thank Dr. Giorgio Carraro (Department of Chemical Sciences, Padova University, Italy) for skillful support and useful discussions.

Conflict of Interest

The authors declare no conflict of interest.

Keywords

ammonia gas sensors, chemical vapor deposition, Fe_2O_3, Mn_3O_4 nanocomposites, ZnO

Received: July 17, 2019
Revised: September 11, 2019
Published online:

[1] N.-J. Choi, J.-H. Kwak, Y.-T. Lim, T.-H. Bahn, K.-Y. Yun, J.-C. Kim, J.-S. Huh, D.-D. Lee, *Sens. Actuators, B* **2005**, *108*, 298.
[2] E. Comini, C. Baratto, I. Concina, G. Faglia, M. Falasconi, M. Ferroni, V. Galstyan, E. Gobbi, A. Ponzoni, A. Vomiero, D. Zappa, V. Sberveglieri, G. Sberveglieri, *Sens. Actuators, B* **2013**, *179*, 3.
[3] A. Ponzoni, E. Comini, I. Concina, M. Ferroni, M. Falasconi, E. Gobbi, V. Sberveglieri, G. Sberveglieri, *Sensors* **2012**, *12*, 17023.
[4] G. Eranna, B. C. Joshi, D. P. Runthala, R. P. Gupta, *Crit. Rev. Solid State Mater. Sci.* **2004**, *29*, 111.
[5] H. Rahaman, S. Kundu, S. K. Ghosh, *ChemistrySelect* **2017**, *2*, 6991.
[6] L. Zhang, G. Wang, F. Yu, Y. Zhang, B.-C. Ye, Y. Li, *Sens. Actuators, B* **2018**, *258*, 589.
[7] J.-H. Kim, J.-H. Lee, A. Mirzaei, H. W. Kim, S. S. Kim, *Sens. Actuators, B* **2018**, *258*, 204.
[8] Z. Deng, G. Meng, X. Fang, W. Dong, J. Shao, S. Wang, B. Tong, *J. Alloys Compd.* **2019**, *777*, 52.
[9] N. Joshi, L. F. da Silva, H. S. Jadhav, F. M. Shimizu, P. H. Suman, J.-C. M'Peko, M. O. Orlandi, J. G. Seo, V. R. Mastelaro, O. N. Oliveira, *Sens. Actuators, B* **2018**, *257*, 906.
[10] L. Sui, X. Song, X. Cheng, X. Zhang, Y. Xu, S. Gao, P. Wang, H. Zhao, L. Huo, *CrystEngComm* **2015**, *17*, 6493.
[11] H. Yu, S. Wang, C. Xiao, B. Xiao, P. Wang, Z. Li, M. Zhang, *CrystEngComm* **2015**, *17*, 4316.
[12] C. Marichy, N. Pinna, *Adv. Mater. Interfaces* **2016**, *3*, 1600335.
[13] G. Sberveglieri, C. Baratto, E. Comini, G. Faglia, M. Ferroni, M. Pardo, A. Ponzoni, A. Vomiero, *Thin Solid Films* **2009**, *517*, 6156.
[14] M. A. Amara, T. Larbi, A. Labidi, M. Karyaoui, B. Ouni, M. Amlouk, *Mater. Res. Bull.* **2016**, *75*, 217.
[15] T. Larbi, L. Ben Said, A. Ben Daly, B. Ouni, A. Labidi, M. Amlouk, *J. Alloys Compd.* **2016**, *686*, 168.
[16] N. John, P. Thomas, K. V. Divya, K. E. Abraham, *Nanotechnology* **2018**, *29*, 335503.
[17] Z. Dong, S. Liu, *J. Mater. Sci.: Mater. Electron.* **2018**, *29*, 2645.
[18] J. Zhang, Z. Y. Qin, D. W. Zeng, C. S. Xie, *Phys. Chem. Chem. Phys.* **2017**, *19*, 6313.
[19] A. Bertuna, G. Faglia, M. Ferroni, N. Kaur, H. M. M. M. Arachchige, G. Sberveglieri, E. Comini, *Sensors* **2017**, *17*, 1000.

[20] P. Chou, H. Chen, I. Liu, C. Chen, J. Liou, K. Hsu, W. Liu, *IEEE Sens. J.* **2015**, *15*, 3711.
[21] H.-I. Chen, C.-Y. Hsiao, W.-C. Chen, C.-H. Chang, T.-C. Chou, I. P. Liu, K.-W. Lin, W.-C. Liu, *Sens. Actuators, B* **2018**, *256*, 962.
[22] J. Zhou, J. Zhang, A. U. Rehman, K. Kan, L. Li, K. Shi, *J. Mater. Sci.* **2017**, *52*, 3757.
[23] N. R. Tanguy, M. Arjmand, N. Yan, *Adv. Mater. Interfaces* **2019**, *6*, 1900552.
[24] H.-J. Kim, J.-H. Lee, *Sens. Actuators, B* **2014**, *192*, 607.
[25] F. Shao, F. Hernández-Ramírez, J. D. Prades, C. Fàbrega, T. Andreu, J. R. Morante, *Appl. Surf. Sci.* **2014**, *311*, 177.
[26] A. A. Najim, H. H. Darwoysh, Y. Z. Dawood, S. Q. Hazaa, A. T. Salih, *Phys. Status Solidi A* **2018**, *215*, 1800379.
[27] N. Barsan, C. Simion, T. Heine, S. Pokhrel, U. Weimar, *J. Electroceram.* **2010**, *25*, 11.
[28] L. Bigiani, C. Maccato, G. Carraro, A. Gasparotto, C. Sada, E. Comini, D. Barreca, *ACS Appl. Nano Mater.* **2018**, *1*, 2962.
[29] T. Zhou, X. Liu, R. Zhang, L. Wang, T. Zhang, *Adv. Mater. Interfaces* **2018**, *5*, 1800115.
[30] C. W. Na, S.-Y. Park, J.-H. Chung, J.-H. Lee, *ACS Appl. Mater. Interfaces* **2012**, *4*, 6565.
[31] A. Ramírez, P. Hillebrand, D. Stellmach, M. M. May, P. Bogdanoff, S. Fiechter, *J. Phys. Chem. C* **2014**, *118*, 14073.
[32] R. Jin, H. Liu, Y. Guan, J. Zhou, G. Li, *CrystEngComm* **2015**, *17*, 7717.
[33] L. Ben Said, A. Inoubli, B. Bouricha, M. Amlouk, *Spectrochim. Acta, Part A* **2017**, *171*, 487.
[34] D. Bekermann, A. Gasparotto, D. Barreca, C. Maccato, E. Comini, C. Sada, G. Sberveglieri, A. Devi, R. A. Fischer, *ACS Appl. Mater. Interfaces* **2012**, *4*, 928.
[35] Q. Simon, D. Barreca, A. Gasparotto, C. Maccato, E. Tondello, C. Sada, E. Comini, G. Sberveglieri, M. Banerjee, K. Xu, A. Devi, R. A. Fischer, *ChemPhysChem* **2012**, *13*, 2342.
[36] D. Barreca, G. Carraro, E. Comini, A. Gasparotto, C. Maccato, C. Sada, G. Sberveglieri, E. Tondello, *J. Phys. Chem. C* **2011**, *115*, 10510.
[37] L. Bigiani, D. Zappa, D. Barreca, A. Gasparotto, C. Sada, G. Tabacchi, E. Fois, E. Comini, C. Maccato, *ACS Appl. Mater. Interfaces* **2019**, *11*, 23692.
[38] L. Yan, Y. Liu, Y. Yan, L. Wang, J. Han, Y. Wang, G. Zhou, M. T. Swihart, X. Xu, *Nano Res.* **2018**, *11*, 520.
[39] Z. Wang, Z. Tian, D. Han, F. Gu, *ACS Appl. Mater. Interfaces* **2016**, *8*, 5466.
[40] L. Bigiani, D. Barreca, A. Gasparotto, C. Sada, S. Martí-Sanchez, J. Arbiol, C. Maccato, *CrystEngComm* **2018**, *20*, 3016.
[41] C. Maccato, L. Bigiani, G. Carraro, A. Gasparotto, C. Sada, E. Comini, D. Barreca, *ACS Appl. Mater. Interfaces* **2018**, *10*, 12305.
[42] G. Karakas, A. Sevinc, *Catal. Today* **2019**, *323*, 159.
[43] G. Liu, J. Hall, N. Nasiri, T. Gengenbach, L. Spiccia, M. H. Cheah, A. Tricoli, *ChemSusChem* **2015**, *8*, 4162.
[44] H. W. Kim, Y. J. Kwon, H. G. Na, H. Y. Cho, C. Lee, J. H. Jung, *Microelectron. Eng.* **2015**, *139*, 60.
[45] D. Barreca, G. Carraro, A. Gasparotto, C. Maccato, T. Altantzis, C. Sada, K. Kaunisto, T.-P. Ruoko, S. Bals, *Adv. Mater. Interfaces* **2017**, *4*, 1700161.
[46] J. F. Moulder, W. F. Stickle, P. E. Sobol, K. D. Bomben, *Handbook of X-ray Photoelectron Spectroscopy*, Perkin–Elmer Corporation, Eden Prairie, MN **1992**.
[47] D. Briggs, M. P. Seah, *Practical Surface Analysis: Auger and X-ray Photoelectron Spectroscopy*, 2nd ed., John Wiley & Sons, New York **1990**.
[48] C. Maccato, L. Bigiani, G. Carraro, A. Gasparotto, R. Seraglia, J. Kim, A. Devi, G. Tabacchi, E. Fois, G. Pace, V. Di Noto, D. Barreca, *Chem. Eur. J.* **2017**, *23*, 17954.
[49] J. Wang, Z. Li, S. Zhang, S. Yan, B. Cao, Z. Wang, Y. Fu, *Sens. Actuators, B* **2018**, *255*, 862.
[50] Pattern No. 024–0734, JCPDS (2000).
[51] S.-K. Lee, D. Chang, S. W. Kim, *J. Hazard. Mater.* **2014**, *268*, 110.
[52] D. Zhang, C. Jiang, P. Li, Y. e. Sun, *ACS Appl. Mater. Interfaces* **2017**, *9*, 6462.
[53] H. Wu, K. Kan, L. Wang, G. Zhang, Y. Yang, H. Li, L. Jing, P. Shen, L. Li, K. Shi, *CrystEngComm* **2014**, *16*, 9116.
[54] D. Zappa, A. Bertuna, E. Comini, M. Molinari, N. Poli, G. Sberveglieri, *Anal. Methods* **2015**, *7*, 2203.
[55] Y. Q. Liang, Z. D. Cui, S. L. Zhu, Z. Y. Li, X. J. Yang, Y. J. Chen, J. M. Ma, *Nanoscale* **2013**, *5*, 10916.
[56] H.-J. Kim, H.-M. Jeong, T.-H. Kim, J.-H. Chung, Y. C. Kang, J.-H. Lee, *ACS Appl. Mater. Interfaces* **2014**, *6*, 18197.
[57] D. A. Shirley, *Phys. Rev. B* **1972**, *5*, 4709.

